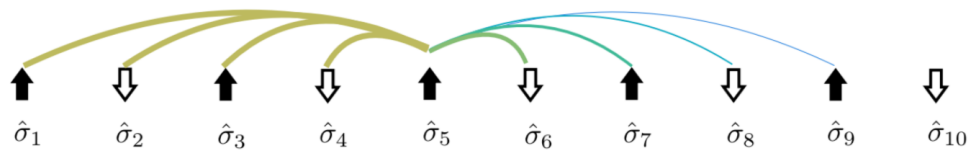




Centre for High Energy Physics, Indian Institute of Science

HE 381: Quantum Field Theory on a Quantum Computer
Instructor: Prof. Aninda Sinha

Quantum Simulations for Schwinger Model



Aman Goyal

Nikshay Chugh

A term paper submitted in partial fulfillment of the requirements for the course
HE 381: QFT on a Quantum Computer

December 1, 2025

Contents

1	Introduction	2
2	Fermionic Simulations	2
2.1	Lattice Theory Basics	2
2.2	Setting Up the Stage	3
2.3	Vacuum Fluctuations	4
2.4	String Breaking	6
2.5	Charge Conserving Trotter Decomposition	7
2.6	Faulty Gates?	8
2.7	AI Usage	9
3	Bosonic Simulations	9
3.1	Theoretical Framework: From Screening to Confinement	9
3.2	Lattice Discretization and Hamiltonian Construction	9
3.3	Real-Time Dynamics: String Breaking vs. Confinement	10
3.4	Static Potential and Charge Screening	11
3.5	Entanglement Entropy in Collisions	11
3.6	High-Energy Scattering Probability	12
3.7	Dynamic Screening and Particle Production	12
3.8	Perturbation Theory Limits	13
3.9	Vacuum Structure and Phase Transitions	13
4	Validation and Detailed Dynamics (Bosonized)	14
4.1	Method Validation: Benchmark vs. Quantum Simulator	14
4.2	Induced Currents and Charge Transport	15
4.3	Meson Scattering Dynamics	16
5	Outlook	16

1 Introduction

The Schwinger Model, defined as Quantum Electrodynamics (QED) in 1+1 dimensions, serves as a pivotal cornerstone in theoretical physics[1]. It describes the interaction between Dirac fermions and an electromagnetic field within a simplified spacetime consisting of only one spatial and one temporal dimension. Despite its apparent simplicity compared to the four-dimensional world, the model exhibits rich, non-perturbative phenomena that are strikingly similar to Quantum Chromodynamics (QCD), the theory governing the strong nuclear force.

We study the Schwinger model primarily because it acts as an ideal “toy model” for understanding the complexities of QCD. It is one of the few gauge theories that shares critical features with the strong force—such as charge confinement, chiral symmetry breaking, and a topological vacuum structure—while remaining mathematically tractable. This unique combination makes it an excellent testing ground for benchmarking numerical techniques, particularly Lattice Gauge Theory. Furthermore, as detailed in this paper, the model is perfectly suited for the emerging field of quantum simulation. By mapping the Schwinger model onto qubit systems, we can probe dynamic properties, such as string breaking and vacuum fluctuations, in real-time, offering insights that are often computationally prohibitive for classical computers in higher-dimensional theories.

2 Fermionic Simulations

2.1 Lattice Theory Basics

In this article, we will utilize Kogut-Susskind’s Hamiltonian formulation for lattice gauge theory, which employs the concept of staggered fermions[2]. In staggered fermions, the degrees of freedom of a spinor are divided into two lattice points. This formulation bypasses the doubling problem of fermions in the continuous limit. The Kogut-Susskind Hamiltonian for 1+1 QED (Schwinger model) is given by

$$H_{\text{KS}}^{1+1} = \frac{i}{2a} \sum_x \left[\phi^\dagger(x) e^{i\theta(x)} \phi(x+a) - \text{h.c.} \right] + m \sum_x (-1)^{x/a} \phi^\dagger(x) \phi(x) + \frac{g^2 a}{2} \sum_x E(x)^2. \quad (2.1)$$

Here $E(x)$ corresponds to the electric and $\theta(x)$ is the gauge field, with the commutation relations given by $[\theta(x_m), E(x_n)] = i\delta_{mn}$. $\phi(x)$ represents the staggered fermionic field. g is the gauge coupling and a is the lattice spacing.

We work in the temporal gauge, i.e., $A^0(x) = 0$. In the continuum theory, transitioning from the Lagrangian formalism to the Hamiltonian formalism, $A^0(x)$ serves as a Lagrange multiplier, corresponding to Gauss's Law equation of motion. Therefore, a physical state must satisfy Gauss's law. On the lattice, this is implemented as follows

$$G(x) = E(x) - E(x-a) - Q(x), \quad \text{where} \quad Q(x) = -\phi^\dagger(x)\phi(x) + \frac{1 - (-1)^{x/a}}{2}. \quad (2.2)$$

Here, we will refer to the operator $G(x)$ as the Gauss operator and $Q(x)$ as the charge operator. Gauss's law on a lattice of a physical state implies

$$G(x)|\psi\rangle_{\text{phy}} = 0 \quad \forall x. \quad (2.3)$$

This is a necessary condition for a physical state. Notice that the form of the charge operator in (2.2) implies that an occupied state at an even site corresponds to an electron and an unoccupied state at an odd site corresponds to a positron, see figure 1.

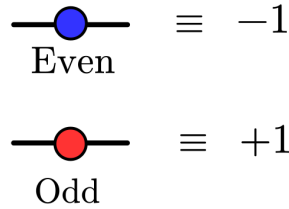


Figure 1: Even occupied site corresponds to an electron and odd unoccupied site corresponds to a positron.

In this section, we have used open boundary conditions, where a background electric field ϵ_0 enters the lattice from the right, and the left end is free. In this boundary condition, the gauge degrees of freedom are not dynamical. They are completely fixed by the fermionic field. We can remove the gauge field terms by performing the following gauge transformation

$$\begin{aligned} \phi(x) &\rightarrow \phi'(x) = \left[\prod_{y < x} U(y) \right] \phi(x), \\ \phi^\dagger(x) &\rightarrow \phi'^\dagger(x) = \left[\prod_{y < x} U(y) \right] \phi^\dagger(x), \\ U(x) &\rightarrow U'(x) = \left[\prod_{y < x} U(y) \right] U(x) \left[\prod_{z \leq x} U(z) \right] = \mathbf{1}. \end{aligned} \quad (2.4)$$

Further, from Gauss's law, we can eliminate the dependence on the electric field. Therefore, we can write the Hamiltonian purely in terms of fermionic fields, and its form is given as follows

$$\begin{aligned} H_{\text{KS}}^{1+1} = & \frac{i}{2a} \sum_{x=0}^{N-2} [\phi(x)^\dagger \phi(x+a) - \text{h.c.}] + m \sum_{x=0}^{N-1} (-1)^{x/a} \phi^\dagger(x) \phi(x) \\ & + \frac{g^2 a}{2} \sum_{x=0}^{N-2} \left(\epsilon_0 + \sum_{y=0}^x \left[-\phi^\dagger(y) \phi(y) + \frac{1 - (-1)^{y/a}}{2} \right] \right)^2. \end{aligned} \quad (2.5)$$

2.2 Setting Up the Stage

To simulate the Hamiltonian (2.5), we need to map the Hilbert space of the fermions to the Hilbert space of qubits. This can be achieved by mapping fermionic operators to the Pauli operators in a way that ensures they follow the correct anti-commutator relations. One such mapping is given by the Jordan-Wigner mapping. The map is given by

$$\phi(x) \rightarrow \left(\prod_{m < n} \sigma_m^z \right) \sigma_n^+, \quad \phi^\dagger(x) \rightarrow \left(\prod_{m < n} \sigma_m^z \right) \sigma_n^-. \quad (2.6)$$

Using this map, the Hamiltonian (2.5) maps to

$$H = \frac{w}{2} \sum_{n=0}^{N-2} (X_n X_{n+1} + Y_n Y_{n+1}) + \frac{\mu}{2} \sum_{n=0}^{N-1} (-1)^{n+1} Z_n + \sum_{n=0}^{N-2} \left(\epsilon_0 + \sum_{m=0}^n \frac{Z_m - (-1)^m}{2} \right)^2. \quad (2.7)$$

Here we have rescaled the Hamiltonian as $H \rightarrow 2/g^2 a H$, therefore $w = 1/g^2 a^2$ and $\mu = 2m/g^2 a$. Notice that the last term introduces cross terms such as $Z_m Z_n$, which corresponds to non-local Coulomb interactions. This is because we have eliminated the electric field using charges, which requires the knowledge of all the charges present on the lattice. At the level of a quantum circuit, this means that we have effectively reduced the width of the quantum circuit, as we no longer have to deal with bosonic degrees, but at the cost of increased circuit depth.

To realize the time evolution of the Hamiltonian (2.7), we decompose the Hamiltonian as follows

$$H = H^{(XX)} + H^{(YY)} + H^{(ZZ)} + H^{(Z)}. \quad (2.8)$$

Therefore, the Trotterized time evolution is given by

$$\tilde{U}(T) = \prod_{i=1}^{N_t=T/t} \left(e^{-itH^{(Z)}} e^{-itH^{(ZZ)}} e^{-itH^{(YY)}} e^{-itH^{(XX)}} \right) \quad (2.9)$$

We can directly read off from (2.7) how to implement this. This quantum circuit realization of one step of the (2.9) is given in the figure 2.

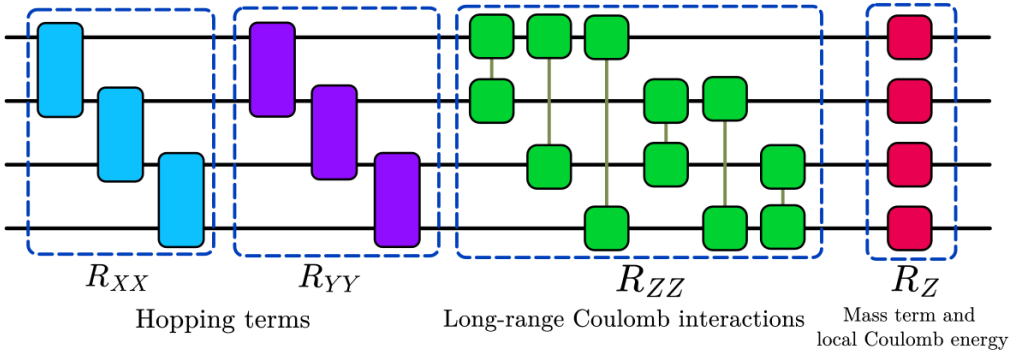


Figure 2: Circuit realization of the time evolution gate.

R_{ZZ} gate can be easily implemented using an R_z and two CNOT gates (done in class), and R_{XX} and R_{YY} can be implemented by rotating the qubits by $R_Y(\pi/2)$ and $R_X(\pi/2)$ respectively.

2.3 Vacuum Fluctuations

We know that the vacuum state of an interacting theory is not static. Particle and anti-particle pairs pop in and out of existence as a virtual particle[3]. Vacuum fluctuation has also been experimentally proven in the form of the Casimir effect[4]. The Schwinger model can serve as a simple toy model to simulate these quantum fluctuations and gain insight into them. In this section, we will discuss how to simulate and study the fluctuations of a quantum computer for the Schwinger model.

The physical vacuum state for the Hamiltonian (2.7) is given by $|0101\rangle$ for 4 qubits. If we time-evolve this state, then we should see small quantum fluctuations in the particle densities. In Figure 3, I have time-evolved the vacuum state using the Trotterization scheme (2.9) and benchmarked it against the exact time-evolution operator. We can observe that there is a small probability (peaking at ≈ 0.25) of observing a particle at the center, which implies the existence of virtual particles.

To separate these virtual particle pairs, we can apply a strong background electric field. This electric field will pull the electron-positron apart and give them enough energy to become a real particle pair. In the figure 4, we can observe from the graphs that as a consequence of the applied electric field, peak particle density is raised up to 0.6 and dipoles are created, signaling that electron-positron pairs are indeed separating from each other. For completeness, I have also applied the electric field toward the negative x-axis. From figure 5, we observe that a strong dipole is created at the center of the lattice, signaling the ripping of the virtual pair particles.

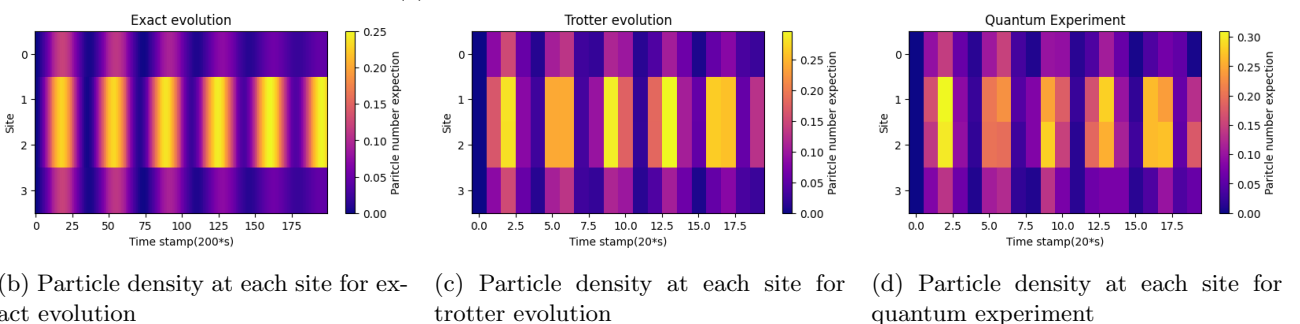
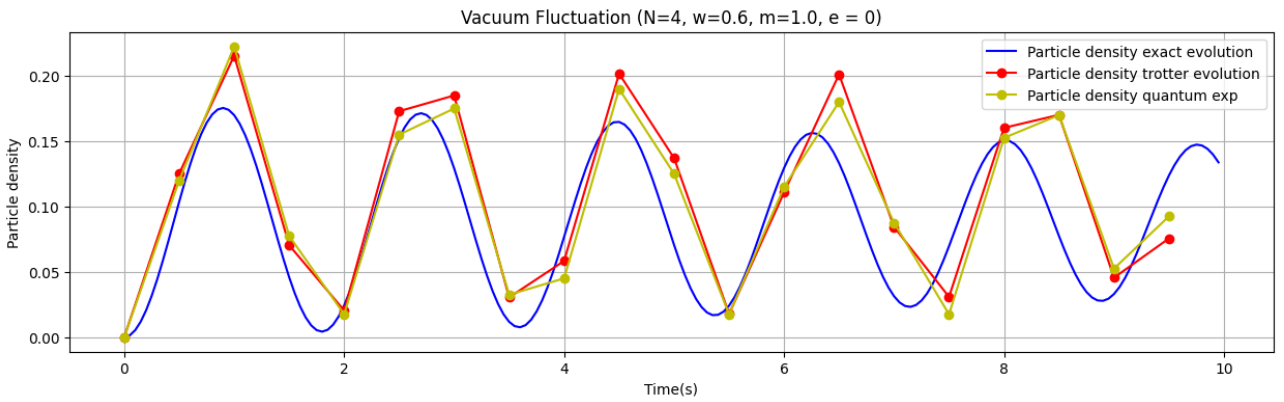


Figure 3: Vacuum state is time evolved using Trotter steps and simulated on a quantum computer. No background electric field is applied in this case. Small particle fluctuations can be observed at the center.

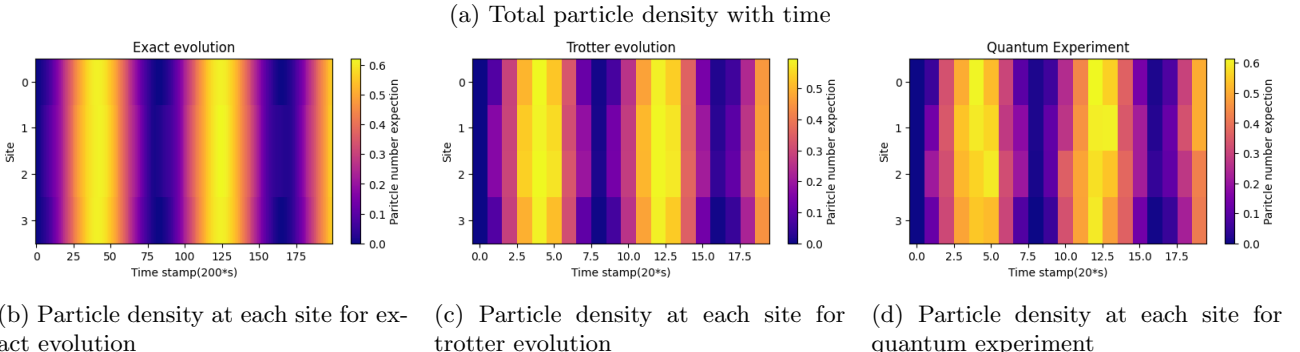
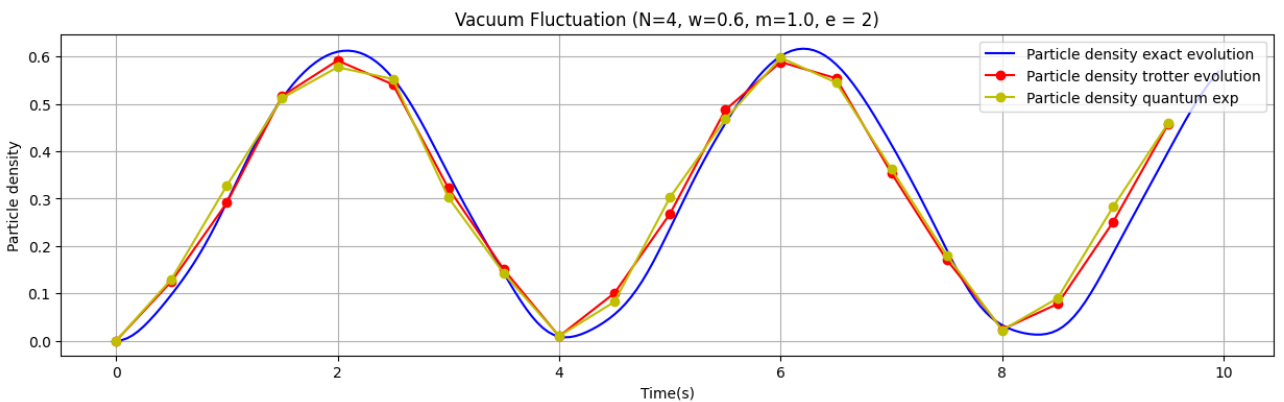
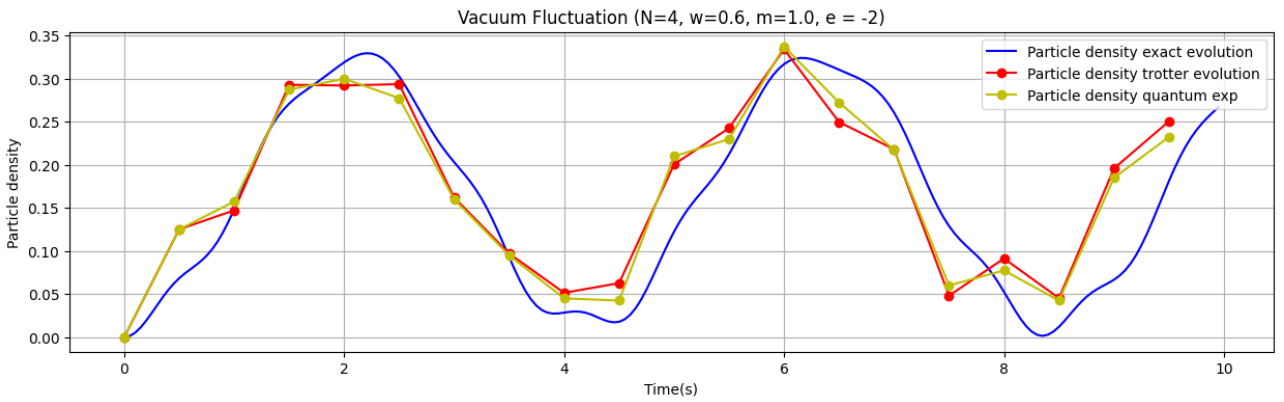
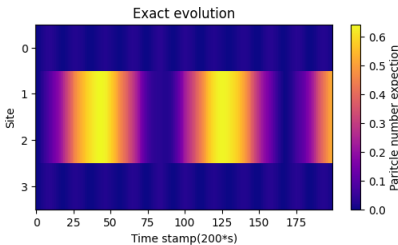


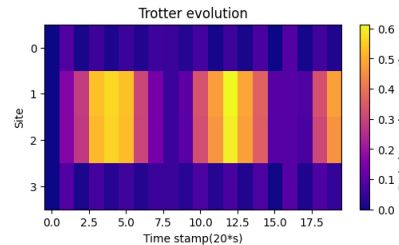
Figure 4: A strong electric field is applied toward the positive x direction. It is observed that this electric field increased the particle densities.



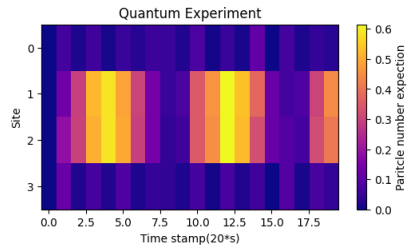
(a) Total particle density with time



(b) Particle density at each site for exact evolution



(c) Particle density at each site for Trotter evolution



(d) Particle density at each site for quantum experiment

Figure 5: Electric field is applied toward the negative x-axis. We see that a strong dipole is created at the center (this is because it is the most favorable state for the applied electric field).

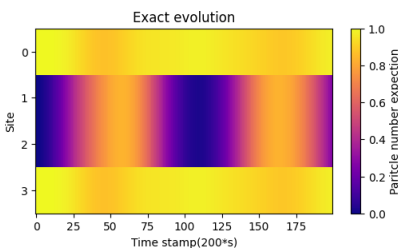
2.4 String Breaking

One of the most interesting features of the Schwinger model is that it exhibits particle confinement. The potential energy between two particles increases linearly in this model. As a consequence, if we try to separate an electron-positron pair, the potential energy of the particles increases with the separation. Ultimately, the energy will increase, making particle pair production more favorable, which leads to the string breaking, see figure 6. Confinement is a prominent feature of QCD. Studying the Schwinger model allows us to test non-perturbative methods used in QCD.

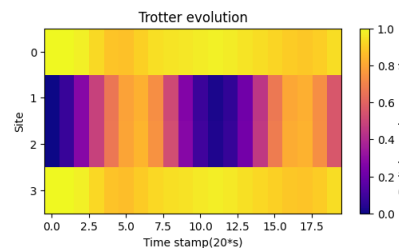


Figure 6: Schematic of string breaking

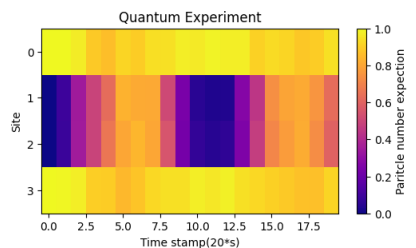
To simulate string breaking using a quantum computer, we start with a state where the electron and positron are separated at the maximum distance possible. For a 4-qubit system, this state is represented by $|1100\rangle$, i.e., an electron is present at site 0, and a positron is present at site 3.



(a) Particle density at each site for exact evolution



(b) Particle density at each site for Trotter evolution



(c) Particle density at each site for quantum experiment

Figure 7: Simulating string breaking ($w = 0.6, m = 0.5, \epsilon_0 = 0.0$)

If we time-evolve this state, we observe that particles appear at the center of the lattice (see figure 7), indicating the breaking of the string. There is an intuitive cross-check we can do here. If we increase the mass of the fermions, then it would require more energy for particle creation; therefore, pair production is less favorable. Hence, we must see a fainter peak at the center of the lattice.

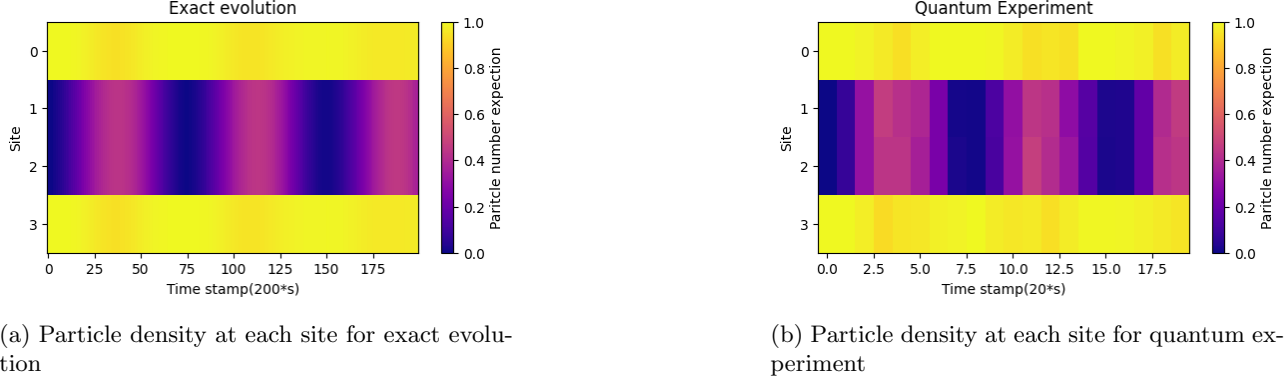


Figure 8: Simulating string breaking ($w = 0.6, m = 1.0, \epsilon_0 = 0.0$)

Figure 8 says exactly this. An increase in fermion mass decreased the probability of the string breaking.

2.5 Charge Conserving Trotter Decomposition

The results so far seem promising, as they align closely with the exact evolution. However, I noticed a flaw in the Trotter time evolution. We started with the assumption that if we begin with a physical state, then it must time-evolve in a physical state. This doesn't seem to be the case with Trotter time evolution.

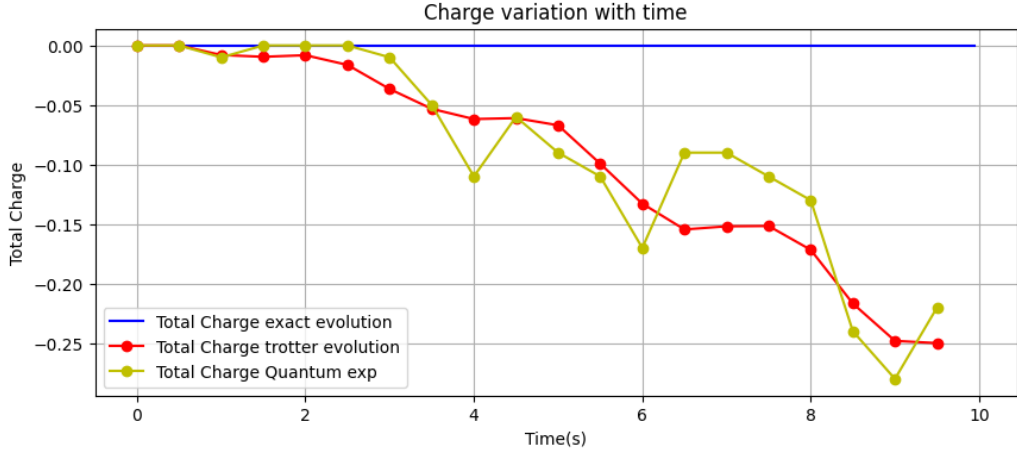


Figure 9: Time evolving the vacuum state ($w = 0.6, m = 0.5, \epsilon_0 = 1.0$)

By examining Figure 9, we observe that even if we initially start with a state of 0 net charge, it begins to accumulate over time. Hence, we drift away from the physical state. Either we must increase the number of Trotter steps or find a suitable decomposition.

The reason behind this drift is that the total charge operator $Q \sim \sum_n Z_n$ doesn't commute with the hopping terms of the Trotter decomposition (2.9). However, I noticed that the sum of charge operators at two constitutive sites commutes with the hopping at those two sites, i.e., for $Q_{n,n+1} \sim Z_n + Z_{n+1}$ we have $[X_n X_{n+1} + Y_n Y_{n+1}, Q_{n,n+1}] = 0$. This means that the charge-conserving Trotter decomposition must have the following form

$$V(T) = \prod_{i=1}^{N_t=T/t} \left(e^{-itH^{(Z)}} e^{-itH^{(ZZ)}} \prod_{n=0}^{N-2} e^{-itw/2(X_n X_{n+1} + Y_n Y_{n+1})} \right). \quad (2.10)$$

However, the question now is how to implement the combined rotation R_{XX+YY} on a quantum circuit. For this, I found that this rotation can be implemented using native gates, as shown in the figure 10.

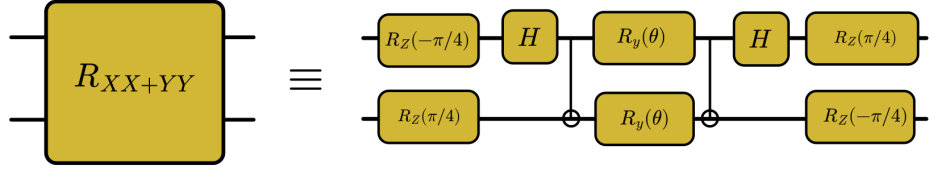


Figure 10: Circuit realization of the gate R_{XX+YY} .

Using this decomposition, we observe that the total charge now remains zero at all times. See figure 11 (Machine errors are present and of the order of 10^{-16}).

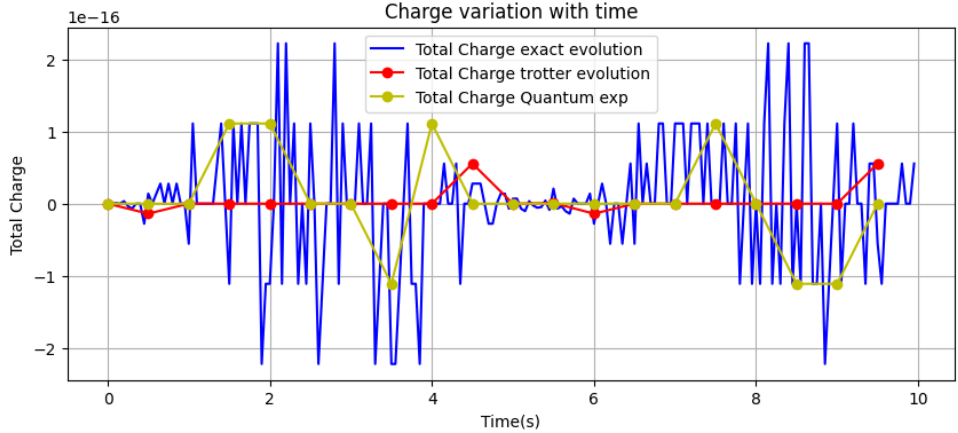


Figure 11: Time evolving the vacuum state using the new Trotter step($w = 0.6, m = 0.5, \epsilon_0 = 1.0$)

2.6 Faulty Gates?

An attempt has been made to simulate noise in the quantum gates using Qiskit. I modeled noise for a specific gate (results for R_Y are presented here) such that it completely randomizes the state of the qubit with some small probability (here taken to be 0.01). The results are as follows.

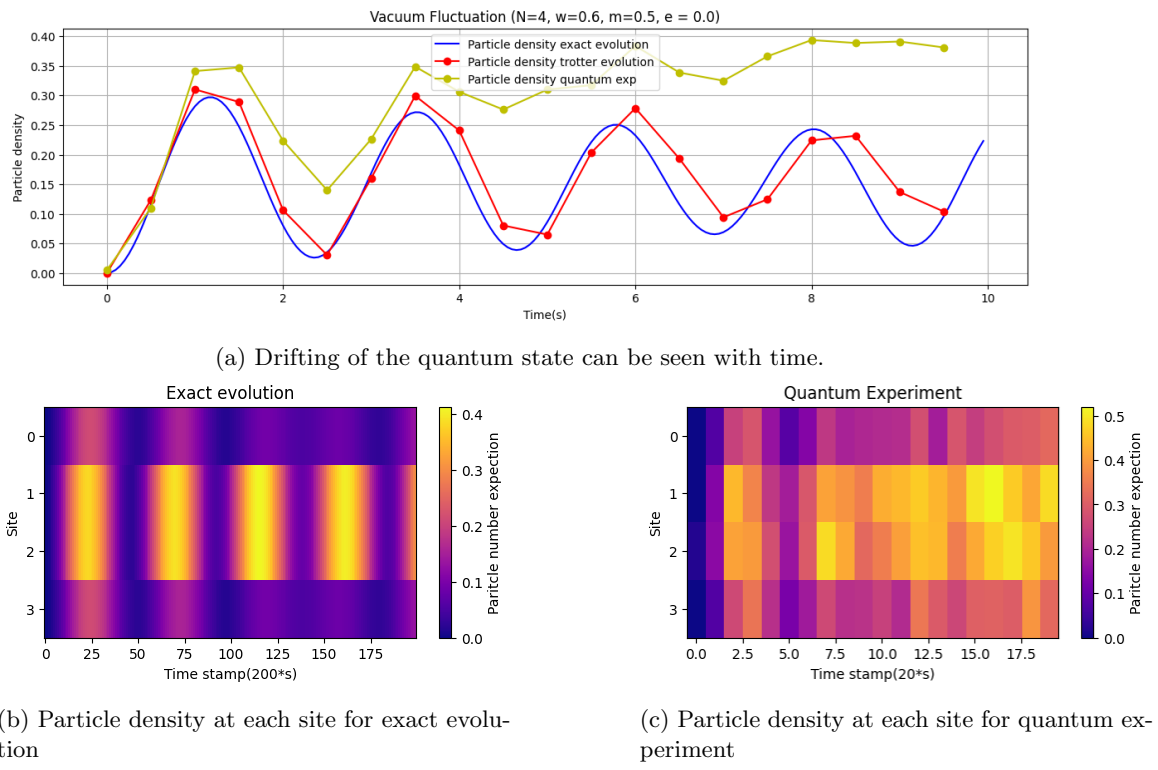


Figure 12: Benchmarking faulty gate against exact evolution ($w = 0.6, m = 0.5, \epsilon_0 = 0.0$)

2.7 AI Usage

I have mostly used Gemini LLM to assist me. I started from scratch and asked it to explain to me what the Schwinger model is, how to implement it on a lattice, and then how to implement it on a quantum computer. It explained everything with a fair amount of detail. The code it provided was not entirely correct (as expected); however, it served as a very good template for me to start coding.

Gemini helped me simplify the cross-terms in (2.7) so that I can write it in terms of Pauli strings and implement it using Qiskit easily. It also helped in building the noise model (that was the last-minute decision).

Neither Gemini nor ChatGPT was able to decompose or verify the combined rotation of $R_{XX,YY}$. I had to find it through painstaking trial and error on Mathematica.

3 Bosonic Simulations

The bosonic formulation offers a powerful alternative to the fermionic lattice gauge theory. By leveraging the bosonization equivalence derived by Coleman, we map the fermionic degrees of freedom to a self-interacting scalar field. This allows us to simulate the Schwinger model using truncated harmonic oscillators, which can be efficiently mapped to qubits, providing a distinct perspective on confinement and scattering phenomena.

3.1 Theoretical Framework: From Screening to Confinement

The non-trivial topology of the $U(1)$ gauge field on a circle (S^1) is important for the Schwinger model. The group of gauge transformations exhibits a non-trivial homotopy structure $\pi_1(U(1)) = \mathbb{Z}$, meaning gauge configurations fall into distinct topological classes labeled by an integer winding number N [5]. “Large” gauge transformations shift this winding number, mapping a vacuum state $|N\rangle$ to $|N+1\rangle$.

To enforce gauge invariance under these large transformations, the physical ground state must be an eigenstate of the shift operator. This defines the θ -vacuum as coherent superposition of the winding number sectors

$$|\theta\rangle = \sum_N e^{-iN\theta} |N\rangle, \quad (3.1)$$

where θ is a parameter representing a background electric field [6].

The dynamics are governed by two conserved generators:

- **Vector Charge (Q):** This is the standard electric charge operator ($Q = N_+ - N_-$). It is gauge-invariant and quantized to integer values on physical states.
- **Chiral Charge (\tilde{Q}_5):** Due to the axial anomaly, the naive chiral charge Q_5 is not conserved. However, the modified chiral charge $\tilde{Q}_5 = Q_5 + \frac{ecL}{\pi}$ is the generator that performs chiral rotations and shifts the vacuum angle θ .

Analytically, the distinction between the massless and massive regimes is governed by the presence of the interaction term in the bosonized Hamiltonian. The Hamiltonian density is:

$$\mathcal{H} = \underbrace{\frac{1}{2}\Pi^2 + \frac{1}{2}(\partial_x\phi)^2 + \frac{1}{2}\mu^2\phi^2}_{\text{Free Massive Boson}} - \underbrace{cm^2 \cos(2\sqrt{\pi}\phi + \theta)}_{\text{Interaction}}, \quad (3.2)$$

where $\mu = e/\sqrt{\pi}$ is the Schwinger mass generated by the chiral anomaly.

In the **massless limit** ($m = 0$), the cosine interaction vanishes. Iso and Murayama demonstrated that this theory is exactly solvable and equivalent to a free massive scalar boson. A non-trivial consequence of this solvability is the screening mechanism: unlike the massive case, the massless vacuum can completely screen external charges of *arbitrary* magnitude, not just integer multiples of the fundamental charge e .

In the **massive limit** ($m \neq 0$), the non-linear cosine term (Sine-Gordon potential) fundamentally alters the spectrum. It creates a barrier to pair production, trapping fractional charges and giving rise to stable, confined meson states.

3.2 Lattice Discretization and Hamiltonian Construction

To implement the theory on a digital quantum computer, we discretize the continuous scalar field $\phi(x)$ and its conjugate momentum $\Pi(x)$ onto a lattice of N sites. Following the implementation in our `BosonicSchwingerModel`

class, we map the local field operators to creation and annihilation operators (a_j, a_j^\dagger) of a harmonic oscillator truncated to N_{levels} basis states (typically $N_{levels} = 4$, requiring 2 qubits per site):

$$\phi_j = \frac{1}{\sqrt{2W_0}}(a_j + a_j^\dagger), \quad (3.3)$$

$$\pi_j = -i\sqrt{\frac{W_0}{2}}(a_j - a_j^\dagger). \quad (3.4)$$

The lattice Hamiltonian is constructed by summing kinetic, mass, and interaction terms. As implemented in the `get_hamiltonian_sparse` method, the total Hamiltonian is:

$$H = \sum_{j=0}^{N-1} \left[\frac{1}{2}\pi_j^2 + \left(\frac{\mu^2}{2} + \frac{1}{a^2} \right) \phi_j^2 \right] - \sum_{j=0}^{N-2} \frac{1}{a^2} \phi_j \phi_{j+1} - \sum_{j=0}^{N-1} \kappa \cos(2\sqrt{\pi}\phi_j). \quad (3.5)$$

For the quantum simulation, these bosonic operators are mapped to Pauli strings. We employ a first-order Trotter-Suzuki decomposition for time evolution, $U(t) \approx \prod e^{-iH_k \delta t}$, where the exponentials of the non-commuting kinetic (H_K), mass (H_M), and interaction (H_{int}) terms are applied sequentially. This is realized in our code using Qiskit's `PauliEvolutionGate`.

3.3 Real-Time Dynamics: String Breaking vs. Confinement

To probe the dynamical properties of the vacuum, we initialize the system in a state representing a local excitation—a "flux tube" or "string"—and observe its evolution.

Methodology: The initial state is prepared by applying a displacement operator $D(\alpha) = \exp(\alpha a^\dagger - \alpha^* a)$ to the vacuum state at specific lattice sites. In our simulation (referencing `get_initial_state_vector`), we apply a displacement of magnitude $\alpha = 1.5$ to the central sites. This creates a coherent state excitation localized in space, mimicking a strong electric field concentration. We then evolve this state under the Hamiltonian for both the massless ($m = 0$) and massive ($m = 0.5$) regimes and measure the local field expectation value $\langle \phi_j(t) \rangle$.

Results and Interpretation: In the massless limit, the theory is equivalent to a free massive scalar boson. Figure 13 shows the resulting "light cone" spreading of the excitation. The rapid decay of the field amplitude $\langle \phi \rangle$ towards zero serves as a clear signature of *string breaking*: the vacuum spontaneously creates massless fermion pairs that screen the external field, dissipating the string's energy.

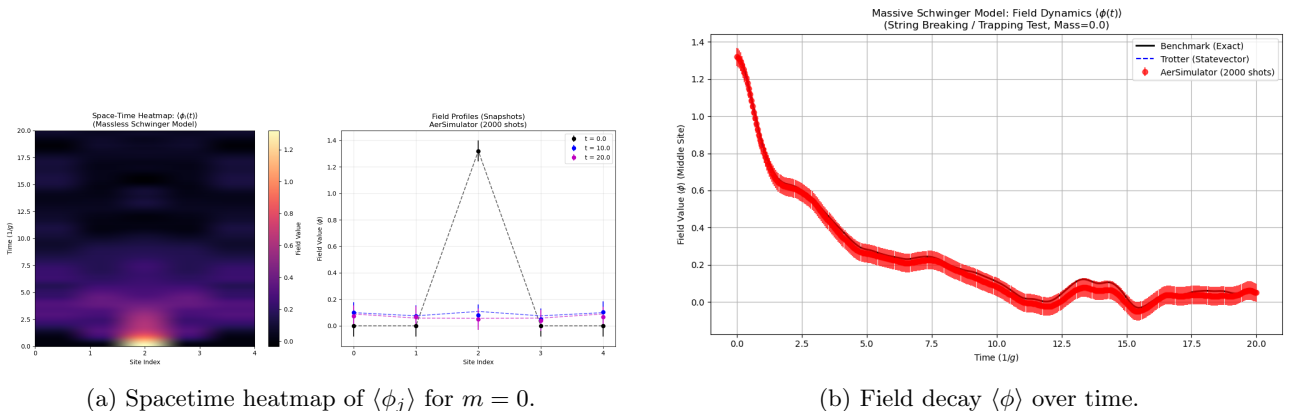


Figure 13: Dynamics in the massless limit. The rapid decay indicates vacuum screening (string breaking) [5].

Conversely, in the massive limit ($m = 0.5$), the cosine potential in the Hamiltonian acts as a barrier. Figure 14 illustrates that the excitation remains spatially localized. The field does not decay to zero but settles into a stable, non-zero oscillation. This persistent "ringing" confirms the phenomenon of *confinement*: the energy of the flux tube is insufficient to generate massive screening pairs, leading to a stable, trapped state [7].

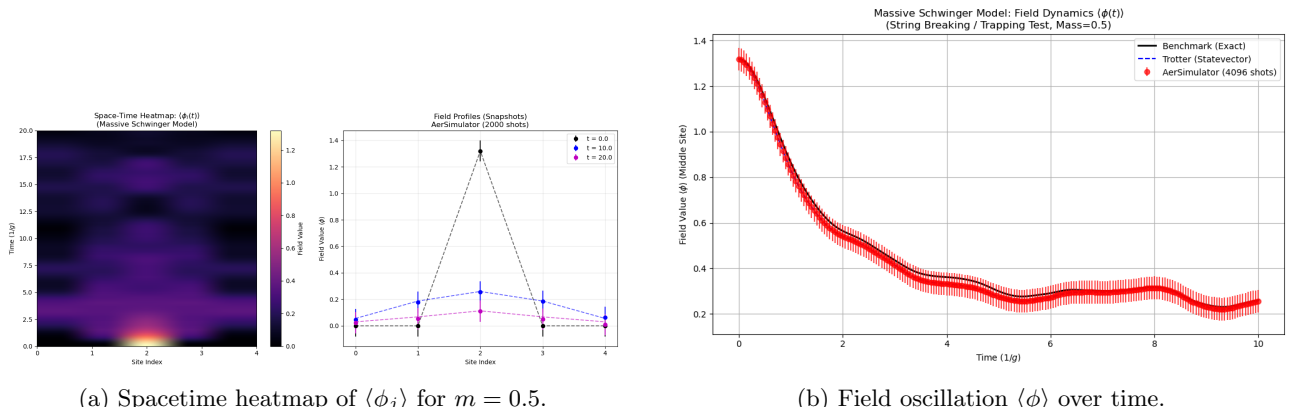


Figure 14: Dynamics in the massive limit. The persistent oscillation signifies a stable, confined flux tube.

3.4 Static Potential and Charge Screening

A definitive test of confinement is the behavior of the static potential between external charges.

Methodology: We calculate the static potential energy $V(L)$ between two external charges $+Q$ and $-Q$ separated by a distance L . This is achieved by modifying the Gauss's law constraint in the Hamiltonian formulation. We compute the ground state energy of the system with these static external charges and subtract the vacuum energy. The calculation is performed for both integer ($Q = 1$) and fractional ($Q = 0.5$) charges.

Results and Interpretation: The results are displayed in Figure 15. For integer charges (blue line), the potential $V(L)$ flattens as separation increases. This indicates *screening*: the vacuum pops pairs out of the vacuum to neutralize the sources, resulting in a short-range force. In contrast, for fractional charges (red line), the potential rises linearly with distance, $V(L) \propto L$. Since the vacuum cannot produce fractional charges to screen the sources, a stable flux tube connects them, leading to *confinement*.

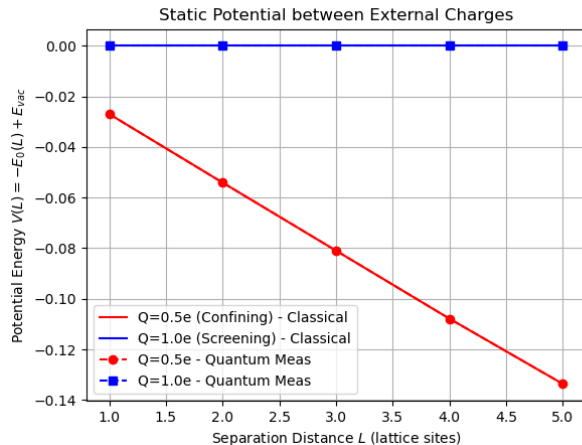


Figure 15: Static potential energy vs. separation distance L . Integer charges are screened (flat potential), while fractional charges are confined (linear potential).

3.5 Entanglement Entropy in Collisions

To understand the quantum correlations generated during particle interactions, we analyze the entanglement entropy.

Methodology: We simulate a collision by initializing two wavepackets with opposite momenta. At each time step of the evolution, we compute the Von Neumann entropy $S_{vN} = -\text{Tr}(\rho_A \ln \rho_A)$ of the reduced density matrix ρ_A for the left half of the lattice. This metric quantifies the quantum information shared between the two halves of the system.

Results and Interpretation: Figure 16 tracks the entropy evolution. During the collision phase ($t \approx 1-4$), we observe a sharp rise in S_{vN} , reflecting the generation of entanglement as the wavepackets interact. Crucially, the entropy does not return to zero post-collision but saturates at a higher value (≈ 2.5). This indicates that the outgoing particles remain entangled, a hallmark of inelastic scattering processes where the quantum state becomes a superposition of multiple outcome channels [8].

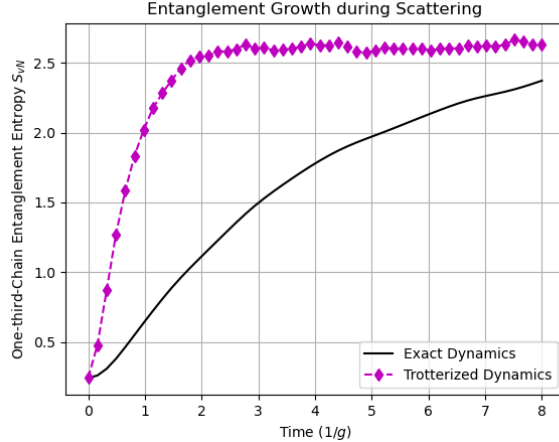


Figure 16: Evolution of entanglement entropy during a meson collision. The saturation post-collision indicates particle production and permanent entanglement.

3.6 High-Energy Scattering Probability

Finally, we probe the elasticity of scattering as a function of collision energy.

Methodology: We prepare initial two-meson states with varying initial momenta k . After evolving the system through the collision, we project the final state back onto the two-particle subspace to determine the elastic scattering probability $P_{\text{elastic}} = |\langle \psi_{\text{final}} | \psi_{\text{elastic}} \rangle|^2$. This requires adiabatically dressing the free momentum eigenstates to the interacting theory to ensure we are scattering physical mesons.

Results and Interpretation: Figure 17 shows the elastic scattering probability against kinetic energy. At low energies, the probability is near unity, indicating purely elastic collisions. As the kinetic energy increases, P_{elastic} drops significantly. This depletion of the elastic channel provides direct evidence of *multiparticle production*: at high energies, the collision creates additional mesons, transferring probability from the elastic sector to inelastic sectors.

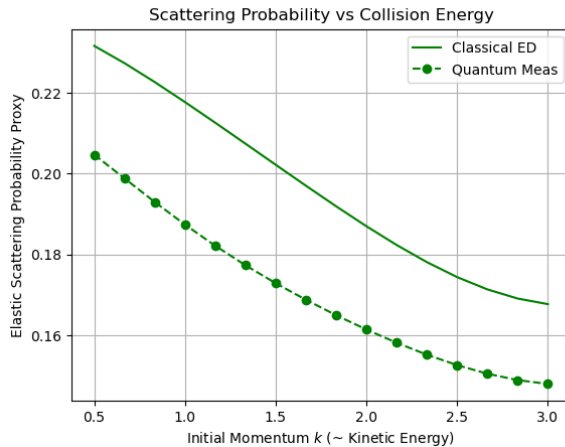


Figure 17: Elastic scattering probability vs. Kinetic Energy. The decrease at high energy signifies the opening of inelastic channels (particle production).

3.7 Dynamic Screening and Particle Production

Beyond static potentials, we investigate the real-time mechanism of screening via a global quench.

Methodology: We initialize the system in the vacuum state of the $\theta = 0$ Hamiltonian. At $t = 0$, we essentially "turn on" a background electric field by evolving this state under the Hamiltonian with $\theta = \pi$. This corresponds to a quench where the topological angle is shifted instantaneously. We track the evolution of the average field $\langle \phi \rangle$ and the total particle number density (meson count) over time.

Results and Interpretation: Figure 18 illustrates the system's response. The local field $\langle \phi \rangle$ (red line) oscillates and decays, indicating that the system is relaxing to screen the new background field. Simultaneously, the particle count (blue line) rises sharply from zero. This is a direct observation of the *Schwinger mechanism*:

the energy stored in the background field is converted into matter (particle-antiparticle pairs), which then act to screen the field.

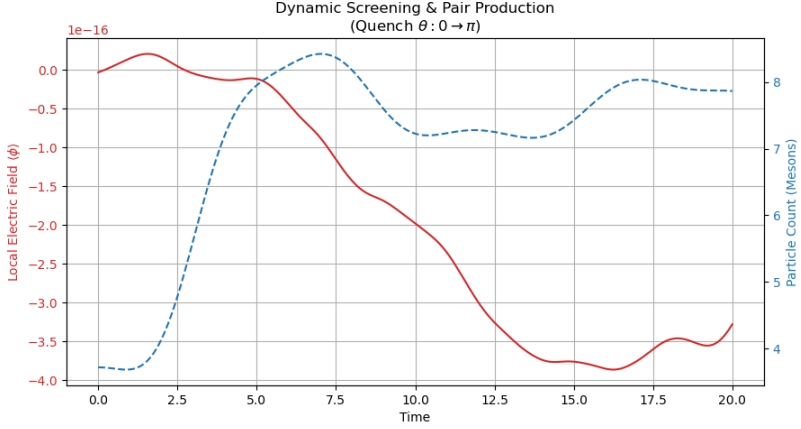


Figure 18: Dynamic screening following a quench to $\theta = \pi$. The decay of the field (red) coincides with the production of particles (blue), demonstrating the conversion of field energy into matter. (Ignore typo 1e-16).

3.8 Perturbation Theory Limits

To validate our simulation across different coupling regimes, we compare our numerical results for the energy gap against analytical perturbation theory.

Methodology: We calculate the energy gap between the first excited state and the ground state ($E_1 - E_0$) for varying values of the fermion mass m and coupling g (where $g \propto e$). We sweep from the weak coupling/massless regime to the strong coupling/massive regime.

Results and Interpretation: Figure 19 demonstrates the convergence to two distinct analytical limits. In the limit $m \ll e$ (left side), the gap approaches the mass of the Schwinger boson, $M = e/\sqrt{\pi}$, derived for the massless theory [6]. In the opposite limit of strong coupling or large mass ($e \ll m$, right side), the gap scales linearly as $2m$, corresponding to the energy required to create a free fermion-antifermion pair. The smooth interpolation between these regimes confirms that our bosonic simulation correctly captures the non-perturbative physics intermediate between these asymptotic limits.

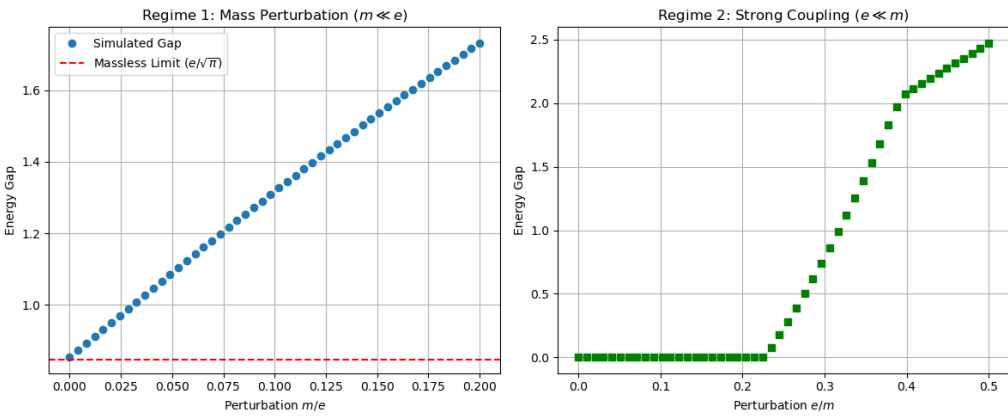


Figure 19: Comparison of the numerical energy gap (blue) with analytical limits. The gap interpolates between the massless Schwinger boson mass ($e/\sqrt{\pi}$) and the massive fermion pair threshold ($2m$).

3.9 Vacuum Structure and Phase Transitions

Finally, we explore the rich topological structure of the vacuum by varying the θ -parameter.

Methodology: We compute the ground state energy density and the chiral condensate $\Sigma = \langle \bar{\psi} \psi \rangle$ as a function of the topological angle θ . In the bosonized language, the chiral condensate maps to the expectation value $\langle \cos(2\sqrt{\pi}\phi) \rangle$. We scan θ over the range $[-\pi, 3\pi]$ to observe periodicity.

Results and Interpretation: The results are summarized in Figure 20. The vacuum energy (left panel) exhibits a clear 2π periodicity, reflecting the topological nature of the $U(1)$ gauge group. Notably, at $\theta = \pi$, the energy shows a non-differentiable cusp. This cusp coincides with a discontinuity in the chiral condensate

(center panel), which jumps abruptly. This behavior signifies a first-order quantum phase transition at $\theta = \pi$, associated with the spontaneous breaking of CP symmetry [6]. The right panel shows the condensate scaling with mass, further validating the massive Schwinger model predictions.

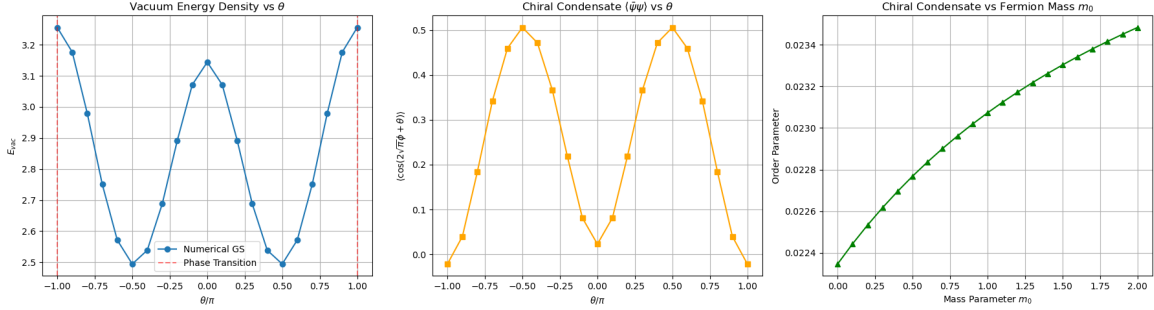


Figure 20: Vacuum structure of the massive Schwinger model. Left: Vacuum energy density vs. θ showing 2π periodicity and cusps at π . Center: Discontinuity in derivative of the chiral condensate at $\theta = \pi$, indicating a phase transition. Right: Dependence of the condensate on mass m_0 .

4 Validation and Detailed Dynamics (Bosonized)

To ensure the reliability of our quantum simulation results, we performed a rigorous validation of our protocols against exact classical benchmarks. We also analyzed fine-grained dynamical quantities like induced currents to gain deeper insight into the charge transport mechanisms.

4.1 Method Validation: Benchmark vs. Quantum Simulator

We compared the time evolution of the system obtained from three distinct methods:

- Exact Benchmark:** Time evolution using exact sparse matrix exponentiation (`scipy.sparse.linalg.expm`) of the full Hamiltonian.
- Trotterized Evolution (Statevector):** Simulation of the quantum circuit using a statevector simulator (noiseless) to validate the Trotter decomposition error ($dt = 0.05$).
- Qiskit Aer Estimator (Shots):** Simulation including shot noise (2000 shots) to mimic the statistical uncertainty of a real quantum device.

System 1: String Dynamics (Breathing Mode) We initialized a "string" state (excitation across sites 3-5) and tracked the field expectation value $\langle\phi_j\rangle$. Figure 21 shows the evolution. The flux tube undergoes a "breathing mode," expanding and contracting. The Trotterized evolution (blue dashed) tracks the exact benchmark (black solid) almost perfectly, confirming that the Trotter error is negligible for our step size. The Aer simulator results (red dots) show statistical scatter but accurately reproduce the dynamics, validating the robustness of the measurement protocol.

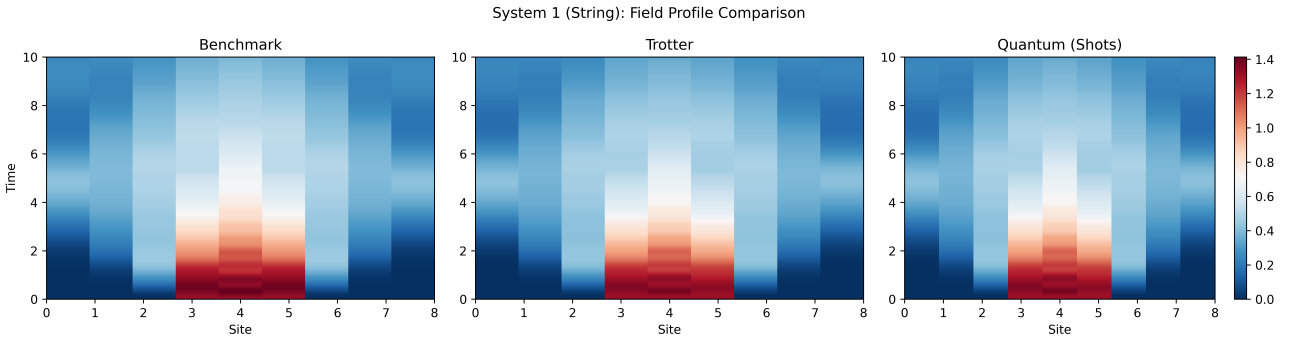


Figure 21: Validation of dynamics for System 1 (String). The quantum simulation methods (Trotter and Aer) show excellent agreement with the exact benchmark, capturing the breathing mode of the flux tube.

System 2: Charge Screening We also validated the screening scenario (System 2), where a single charge is placed at site 4. Figure 22 displays the results. The field decays rapidly as the vacuum screens the charge. Again,

the quantum simulation methods faithfully reproduce the exact features, including the "ringing" oscillations characteristic of massive particle production during screening.

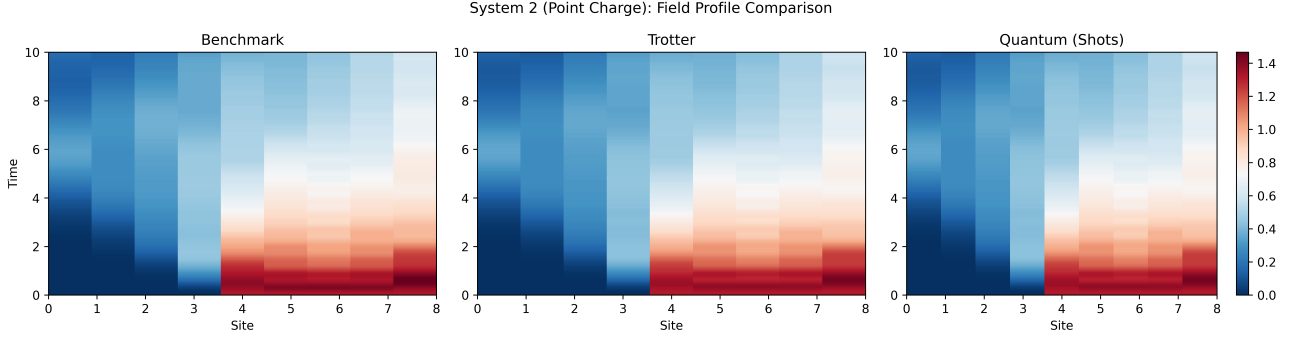


Figure 22: Validation of dynamics for System 2 (Screening). The decay and subsequent oscillation of the field are accurately captured by the quantum simulator.

4.2 Induced Currents and Charge Transport

To understand the microscopic mechanism of screening and transport, we analyzed the current flow across the lattice bonds. The current operator on bond $(j, j + 1)$ is defined via the continuity equation $\partial_t \rho + \nabla J = 0$. In the lattice formulation, this corresponds to the hopping term $J_{j,j+1} \propto i(\phi_j \pi_{j+1} - \pi_j \phi_{j+1})$.

Mid-Bond Current: Figure 23 shows the current accumulation at the exact center of the lattice (Bond 4).

- **System 1 (String):** The current exhibits sharp "beating" patterns. These correspond to the wavefronts of the breathing string reflecting off the open boundaries of the lattice (sites 0 and 8) and interfering at the center.
- **System 2 (Screening):** The current shows a deep negative dip followed by damped oscillations. The dip signifies the rapid inflow of vacuum charges to screen the central external charge (vacuum polarization). The subsequent ringing follows a Bessel function behavior $J_0(Mt)$, characteristic of massive scalar dynamics in 1+1D.

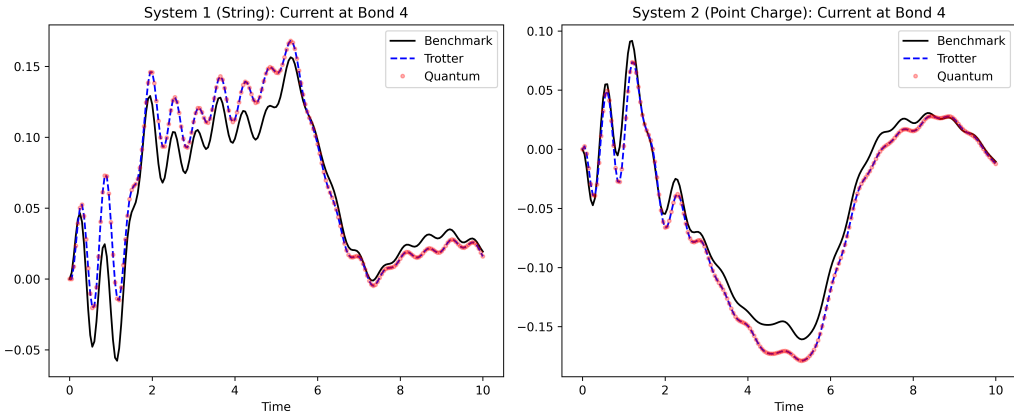


Figure 23: Mid-bond current dynamics. System 1 shows boundary reflections (beating), while System 2 shows a polarization dip followed by massive particle ringing.

Induced Current Profile: The global flow of current is visualized in Figure 24. This plot tracks the current across all bonds over time. We observe the causal propagation of charge (light cone) and the specific flow patterns that lead to the neutralization of the initial electric flux.

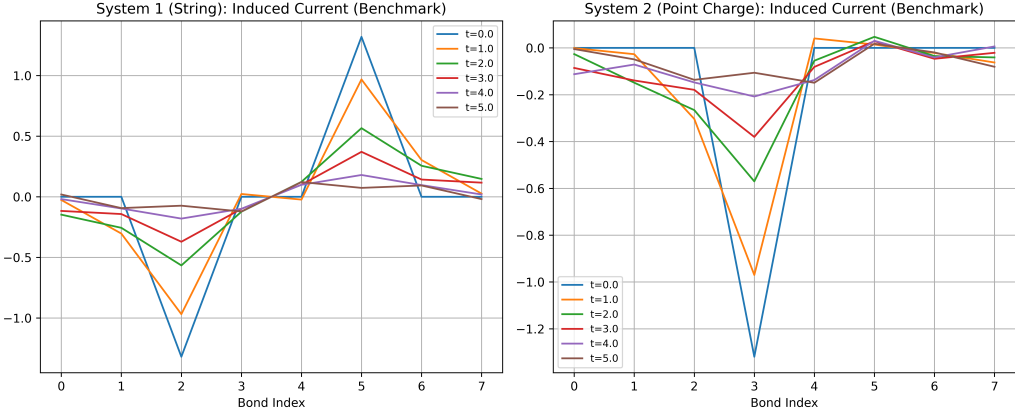


Figure 24: Induced current across the lattice. This metric tracks the vacuum response and the transport of charge required to screen the external field.

4.3 Meson Scattering Dynamics

Finally, we present the full spacetime evolution of the meson scattering experiment discussed in Section 3.5. We initialized two meson wavepackets with momenta k and $-k$ at two sites of the lattice and evolved them under the interacting Hamiltonian. The states were prepared by ASP.

Figure 25 visualizes the collision.

- **Approach ($t < 2.5$):** The two distinct wavepackets (high density regions) propagate ballistically towards the center.
- **Interaction ($t \approx 2.5$):** The packets merge into a single high-density region. The interference pattern here encodes the interaction physics.
- **Scattering ($t > 2.5$):** The wavepackets emerge and spread. The broadening and complex structure of the outgoing waves are signatures of the scattering phase shift and inelastic particle production. This pattern repeats because of confinement and the charges are not screened (though it diffuses slightly, that is the error in ED).

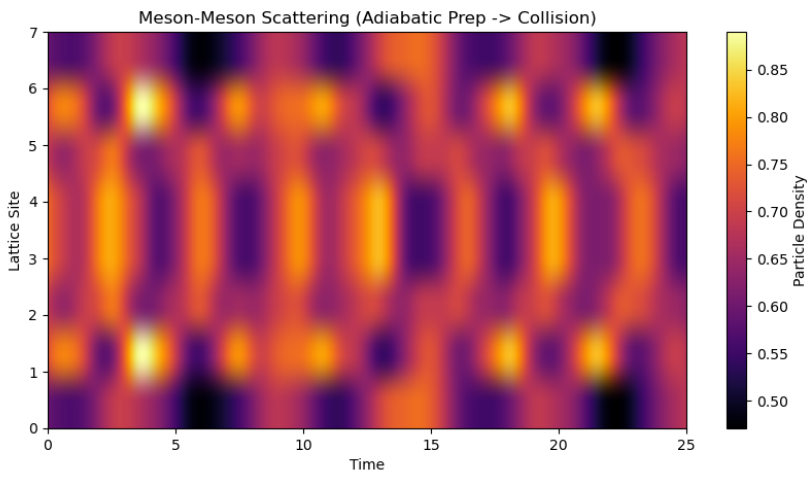


Figure 25: Spacetime heatmap of Meson Scattering. Two wavepackets collide at the center. The interaction creates a complex interference pattern indicative of scattering and entanglement generation.

5 Outlook

In this work, we successfully implemented and benchmarked digital quantum simulations for the Schwinger model using both the Kogut-Susskind fermionic formulation and the Coleman bosonized scalar formulation. By exploiting the duality between these representations, we provide a comprehensive picture of non-perturbative

phenomena in $1 + 1$ -dimensional abelian gauge theory.

Our simulations definitively distinguished between the two fundamental dynamical regimes of the theory. In the massless limit, we observed the phenomenon of *string breaking* and the complete screening of external charges via vacuum polarization, consistent with the exact solution of the massless Schwinger model. Conversely, in the massive regime, we verified the mechanism of *quark trapping*, observing stable flux tubes and a linear static potential for fractional charges, validating Coleman's predictions regarding the phase structure of the massive theory. Furthermore, our analysis of entanglement entropy during meson scattering provided a clear quantum signature of inelastic particle production, a feature inaccessible to classical perturbative methods.

Looking forward, the natural extension of this work is the simulation of gauge theories in higher dimensions, specifically $2 + 1$ dimensions, where magnetic effects and plaquette terms introduce significantly richer physics. Additionally, extending the bosonic formulation to non-Abelian gauge theories (such as $SU(2)$ or $SU(3)$) remains a critical challenge for simulating Quantum Chromodynamics (QCD). Finally, as circuit depths increase to capture long-time dynamics, the integration of error mitigation techniques will be essential to suppress Trotter and gate errors, paving the way for quantum advantage in high-energy physics.

References

- [1] Julian Schwinger. "Gauge Invariance and Mass. II". In: *Phys. Rev.* 128 (5 Dec. 1962), pp. 2425–2429. DOI: [10.1103/PhysRev.128.2425](https://doi.org/10.1103/PhysRev.128.2425). URL: <https://link.aps.org/doi/10.1103/PhysRev.128.2425>.
- [2] John Kogut and Leonard Susskind. "Hamiltonian formulation of Wilson's lattice gauge theories". In: *Phys. Rev. D* 11 (2 Jan. 1975), pp. 395–408. DOI: [10.1103/PhysRevD.11.395](https://doi.org/10.1103/PhysRevD.11.395). URL: <https://link.aps.org/doi/10.1103/PhysRevD.11.395>.
- [3] Matthew D. Schwartz. *Quantum Field Theory and the Standard Model*. Cambridge University Press, Mar. 2014. ISBN: 978-1-107-03473-0, 978-1-107-03473-0.
- [4] S. K. Lamoreaux. "Demonstration of the Casimir Force in the 0.6 to $6\mu\text{m}$ Range". In: *Phys. Rev. Lett.* 78 (1 Jan. 1997), pp. 5–8. DOI: [10.1103/PhysRevLett.78.5](https://doi.org/10.1103/PhysRevLett.78.5). URL: <https://link.aps.org/doi/10.1103/PhysRevLett.78.5>.
- [5] Satoshi Iso and Hitoshi Murayama. "ALL ABOUT THE MASSLESS SCHWINGER MODEL". In: (July 1988).
- [6] Sidney Coleman. "More about the massive Schwinger model". In: *Annals of Physics* 101.1 (1976), pp. 239–267. ISSN: 0003-4916. DOI: [https://doi.org/10.1016/0003-4916\(76\)90280-3](https://doi.org/10.1016/0003-4916(76)90280-3). URL: <https://www.sciencedirect.com/science/article/pii/0003491676902803>.
- [7] Sidney Coleman, R Jackiw, and Leonard Susskind. "Charge shielding and quark confinement in the massive schwinger model". In: *Annals of Physics* 93.1 (1975), pp. 267–275. ISSN: 0003-4916. DOI: [https://doi.org/10.1016/0003-4916\(75\)90212-2](https://doi.org/10.1016/0003-4916(75)90212-2). URL: <https://www.sciencedirect.com/science/article/pii/0003491675902122>.
- [8] Zohreh Davoudi. "TASI/CERN/KITP Lecture Notes on "Toward Quantum Computing Gauge Theories of Nature"". In: (July 2025). arXiv: [2507.15840 \[hep-lat\]](https://arxiv.org/abs/2507.15840).